Catalytic locomotion of Au/Ru core-shell nanowire motors

Bumjin Jang„ Wang Wei, Samuel Wiget„ Petruska J. Andrew, Xiangzhong Chen„ Chengzhi Hu„ Ayoung Hong„ David Folio, Antoine Ferreira, Salvador Pané, et al.

▶ To cite this version:

Bumjin Jang„ Wang Wei, Samuel Wiget„ Petruska J. Andrew, Xiangzhong Chen„ et al.. Catalytic locomotion of Au/Ru core-shell nanowire motors. ACS Nano, 2016, 10 (11), 10.1021/acsnano.6b04224 . hal-01410107

HAL Id: hal-01410107

https://hal.science/hal-01410107

Submitted on 26 Jan 2017

Catalytic locomotion of Au/Ru core-shell nanowire motors

Bumjin Jang,*[†] Wei Wang,[‡] Samuel Wiget,[†] Andrew J. Petruska,[†] Xiang-Zhong Chen,[†] Chenzhi Hu,* [†] *David Folio,*[§] *Antoine Ferreira,* [§] *Salvador Pané,** [†] *and Bradley J. Nelson*[†]

[†]Institute of Robotics and Intelligent Systems, ETH Zurich, Zurich, CH-8092, Switzerland

[‡]Shenzhen Key Laboratory for Advanced Materials, School of Material Sciences and Engineering, Shenzhen Graduate School, Harbin Institute of Technology, University Town, Shenzhen 518055, China

[§] INSA Centre Val de Loire, Universite d'Orléans, PRISME EA 4229, Bourges, France.

KEYWORDS: *core-shell nanowires, catalytic micro-nanomotors, self-electroosmosis, self-diffusiophoresis, net propulsive force*

Fifteen years ago, Whitesides et al. pioneered a work on self-propelled catalytic millimeter-scale ships,[1] triggering a mighty development of synthetic micro- and nanomotors. These devices move autonomously in the presence of a fuel solution by converting chemical to mechanical energy.[2] Most of reported catalytic micro- and nanomotors are driven by the decomposition of hydrogen peroxide, although there are other recent examples using glucose and urea as fuels.[3-5] Several applications for these miniaturized motors have been demonstrated such as electronic circuit healing,[6] biosensing,[4, 7] nanolithography,[8] microfluidic pumping,[9] nanocargo transport[10], or environmental remediation (for details, see recent review articles[11-16]). Most of these applications require a precise control over the speed and directionality of the motors.[17], which are highly dependent on the motor design parameters, such as its geometry, size and composition. Understanding the mechanisms involved in the propulsion of catalytic micro- and nanomotors as a function of their design is crucial for controlling their motion. Different propulsion mechanisms have been identified, such as bubble propulsion, self-electroosmosis, self-diffusiophoresis or interfacial tension.[16] In the first mechanism, bubbles are formed on the catalytic surface and impart momentum to the motor. For example, tubular microjets[18, 19] are driven by oxygen bubble propulsion, caused by the decomposition of H_2O_2 at the inner catalytic surface. While bubble propulsion seems at first glance the most intuitive way to explain the motion of these motors, this mechanism cannot be used to rationalize, for instance, the motion of bimetallic structures such as Pt/Au or Cu/Pt nanowires (NWs) in H_2O_2 and I_2 solutions respectively.[20, 21] For bimetallic NWs, self-electroosmosis [22, 23] is generally the most accepted mechanism compared to others[21],[24]. In this case, a self-induced electric field is generated by redox reactions occurring on the two different metallic segments. The motion of other micro- and nanomotors has been explained in terms of self-diffusiophoresis. Several works suggest that micro- and nanoparticles asymmetrically coated with Pt move due to an O_2 concentration gradient, caused by the asymmetric decomposition of H_2O_2 along the body of the motor.[25-27] [28, 29] Recent investigations evaluating more complex motor architectures are pointing towards a concomitant occurrence of mechanisms.[30, 31]

Among all micro- and nanomotors' structures, NWs are particularly appealing due to their unique physical properties.[32] Additionally, NWs can be compartmentalized in several functional modules by means of segmentation[33] or coaxial lithography[34] to increase their capabilities and functionalities. For instance, the trajectory of catalytic NW motor consisting of Pt/Ni/Au/Ni/Au segments can be controlled by means of magnetic fields.[35] However, interfacing certain building blocks can be detrimental for several applications. For example, the combination of two dissimilar metallic segments such as Au and Ni can lead to an increase of the corrosion rate of the magnetic part due to galvanic coupling.[36] Also, the interaction of certain materials (e.g. Ni) with the surrounding environment (e.g.biological or aquatic media) must be avoided to prevent undesired leakage of toxic ions. Alternatively, core-shell arrangements can provide an inert housing to prevent certain components to be in direct contact to the surrounding environment. Core-shell NWs have been manufactured using a wide variety of methods, and usually they imply two or more steps.[37-42]

In this work, we capitalize on a recently developed method, which allows for the batch fabrication of freestanding NWs based on template-assisted electrodeposition and wafer bonding. As the NWs are self-supported on the wafer after template removal, a second electrodeposition step can be realized to produce a core-shell architecture. This newly developed method can be adopted to fabricate core-shell NWs with various material combinations. Here, we have produced different types of bimetallic core-shell NWs such as Au/Ru, Rh/Au, Au/Rh and we have investigated for the first time their motion in H_2O_2 solutions. We observed abnormal behaviors of these core-shell devices including a speed increase with the length of Au/Ru core-shell NWs and a large speed difference among Au/Ru, Rh/Au and Au/Rh, which have not been observed for the segmented (conventional bimetallic) NWs. The experimental results suggest that self-electroosmosis cannot be the sole mechanism for the locomotion of these architectures. Indeed, we suggest that self-diffusiophoresis is additionally playing a role as well. Additionally, magnetically guided motion of a (Au-Ni)/Ru core-shell NW is demonstrated. In this configuration, the magnetic component is enclosed within the shell, thus preventing the Ni core to be in contact with the surrounding solution.

Results

Numerical model of electroosmotic mechanism on core-shell NWs. It has previously been established that the electroosmotic force is the main driving force for locomotion of nanomotors based on surface redox reactions.[43, 44] The redox reaction consists of an oxidation reaction and reduction reaction as illustrated in Figure 1a. Protons, oxygen molecules, and electrons are generated in the oxidation process at the anode (Au) by decomposing H_2O_2. The generated protons travel by convection, diffusion, and migration to the cathode (Ru), where they react with electrons, oxygen and H_2O_2 molecules to produce H_2O in the reduction process. As a consequence of this redox reaction, protons are asymmetrically distributed around the nanomotor and, accordingly, an asymmetric electric field is developed. This self-generated electric field causes protons to migrate inside the electrical double layer that naturally formed when the nanomotor is immerged in a water solution. The proton migration leads to an electroosmotic flow, which eventually causes the motion of the nanomotor. The influence of the electroosmotic mechanism on the locomotion of our newly designed nanomotor is simulated using commercial multiphysics simulation package COMSOL (5.1). Figure S1a shows that the proton concentration around the Au/Ru core-shell NW is highly asymmetric, as expected. The protons are highly concentrated at the Au (anode) end the NW, where they are generated, and have a low concentration at the Ru (cathode) end, where they are consumed. As expected, Figure S1b shows that the electric potential is also asymmetric because of the asymmetric distribution of protons. Figure 1b shows that the fluid flows from the anode to the cathode, translating to a directional motion of the Au/Ru core-shell NW with the anode forward. The simulation also reveals that the fluid speed is highest at the interface between the cathode and anode of the core-shell NW, where the majority of the electroosmosis flow occurs.

We notice in our simulation (Figure 1b) that near the opposite tip to the anode there is a convergent flow loop on each side of the rod due to the coupling between the electrosmotic flow moving from the anode to the cathode, and a flow from the surrounding solution due to the electric field pointing towards the cathode. We further investigate how the length of Au/Ru core-shell NW affects the convergent flow. When the length is small enough (~ 500 nm, Figure 1b (i)), the electric field generated at the anode dominates the overall electroosmotic flow (Figure S1c), and the disturbance to the fluid flow at the tip of the cathode is negligible. At approximately 1.5 µm, a flow reversal at the tip occurs, which is caused by the migration of protons from the surrounding solution to the cathode (Figure 1b (ii)). The reverse flow gains enough strength to create vortices near the surface of the NW tip. Further increase in length increase the size of vortices (Figure 1b (iii), (iv)). These vortices represent a local increase in the fluidic drag at the tail of the NW, according to the observed negative fluidic speed at the tip of the cathode as seen from the fluid profile along the NW long axis (Figure S1d).

The nanomotor speeds are calculated from the fluid velocities around the core-shell NWs using the Solomentsev and Anderson model.[45] Figure 1c shows the speed as a function of length of the core-shell NW. The decreased speed with length in the numerical simulation can be attributed to the increase in drag force of the nanomotor as its length increases, since no-slip boundary condition was chosen for the nanomotor surface in the simulation.

Design and fabrication of the Au/Ru core shell NWs. The fabrication process is illustrated in Figure 2a. First, an anodic aluminium oxide (AAO) membrane was transferred onto a Si substrate via the Au/Au compressive bonding technique previously developed in our group.[46] Next, Au was electrodeposited into the pores of the AAO. The AAO was then chemically etched to obtain a freestanding Au NW array on the Si substrate. Ru was then electrochemically deposited on the freestanding Au NW array, hence the formation of a core-shell structure. The strong adhesion between the freestanding array and the Si substrate is able to withstand the electrophoretic and fluidic forces exerted on the NWs during Ru electrodeposition. We importantly note that the freestanding NWs must be kept in solution to prevent drying, because the surface tension forces during drying will cause severe NW aggregation [47] and result in a non-uniform deposition of the Ru shell. After the Ru deposition, the NWs are released by sonication.

A scanning electron microscope (SEM) image obtained using a back-scattered electron (BSE) detector in Figure 2b shows a typical Au/Ru core-shell NW with an approximate diameter and a length of 350 nm and 2.5 μm, respectively, where the length varies with the deposition time of the Au core. Since the intensity of the BSE signal is proportional to the atomic number, the bright area and the dark area can be assigned to Au and Ru, respectively. The Au core appears only at the base (left end) as a consequence of being released from the Si substrate. No obvious defects are observed in the Au/Ru core-shell NW structure as is seen in the high-angle annular dark field (HAADF) scanning transmission electron microscopy (STEM) image (Figure 2c). The corresponding energy dispersive X-ray (EDX) mapping verifies that the core-shell NW is composed of Au and Ru (Figure 2d). For a better understanding of the Ru distribution, we further selectively etched the Au core in Au etchant. Representative SEM and STEM images (Figure 2e,f) show that the remaining structure after etching is a Ru shell. The Ru shell has an approximate diameter of 350 nm, which is similar to that of a Au/Ru core-shell NW. A smooth surface of the nanoshell without holes or cracks on the rod is observed and confirms the uniform distribution and the conformal growth of the Ru shell. Subsequent EDX mapping verifies that the nanoshell solely consists of Ru (Figure 2g).

Catalytic propulsion of the Au/Ru core-shell NWs. The catalytic locomotion of the Au/Ru core-shell NWs (approximate length of 2.5 μm) in H_2O_2 solution was investigated at various concentrations (0, 0.1, 0.3, 2.5, 5, 10 and 20 wt %). As expected, the speed of the core-shell NW increases with the concentration of H_2O_2 (Figure 3a), showing the maximum speed of 41 ± 7.6 μm/s at 20 wt % H_2O_2. The positive correlation between the speed of the motor and the concentration of H_2O_2 is in accordance with previous findings.[48-51] A representative core-shell-NW trajectory is shown in Figure 3a (i). A large displacement is observed over 4.55 sec in the presence of H_2O_2 (5 wt %) in contrast to the control experiment, conducted in the absence of H_2O_2, which shows Brownian motion and a very small displacement (Figure 3a (ii)).

To systematically understand the locomotion, we studied the dynamic motion behavior of the core-shell NW with different lengths (1.8, 2.6 and 3.4 μm). We calculated the mean-square displacement (MSD) from the recorded motion trajectory (see also supporting movie1) using:

$$\Delta L^2(t) \equiv \left\langle \left[r(t) - r(0) \right]^2 \right\rangle \qquad (1)$$

where $r(t) = (x(t), y(t))$.

Similar to catalytic motors of other shapes, the MSD curves in Figure 3b and S2a,b show sinusoidal oscillations, which indicate that our motors exhibit a circular motion.[48, 52, 53] The translational velocity (v), rotational velocity (ω), translational diffusivity (D) and rotational diffusivity (D_r) for a moving particle can be extracted by fitting the MSD curves with[53]:

$$\Delta L^2(t) = 4D_t + \frac{2v^2 D_r t}{D_r^2 + \omega^2} + \frac{2v^2(\omega^2 - D_r^2)}{D_r^2 + \omega^2} + \frac{2v^2 e^{D_r t}}{(D_r^2 + \omega^2)^2}\left[(D_r^2 - \omega^2)\cos\omega t - 2\omega D_r \sin\omega t\right]$$

For comparison, the translational diffusivity $D_{t,b}$ and the rotational diffusivity $D_{r,b}$ of passive Brownian motion (i.e. in the absence of H_2O_2) of our core-shell NW are calculated by the Einstein relation:

$$D_{t,b} = \frac{k_B T}{f_{t,}^{\parallel}} \tag{3}$$

$$\Delta L^2(t) = 4D_t + \frac{2v^2 D_r t}{D_r^2 + \omega^2} + \frac{2v^2(\omega^2 - D_r^2)}{D_r^2 + \omega^2} + \frac{2v^2 e^{D_r t}}{(D_r^2 + \omega^2)^2}\left[(D_r^2 - \omega^2)\cos\omega t - 2\omega D_r \sin\omega t\right] \tag{4}$$

where k_B is the Boltzmann constant, T is the absolute temperature, $f_t^{\parallel}$ is the translational frictional drag force and $f_r^{\parallel}$ is the rotational frictional drag force parallel to the long axis of NW with a length (L) and a diameter (d) in a viscous media $D_{t,b} = \frac{k_B T}{f_{t,}^{\parallel}}$. $D_{r,b} = \frac{k_B T}{f_r^{\parallel}}$ are defined as:[54]

$$f_t^{\parallel} = \frac{2\pi\eta L}{\ln(L/d) - 0.207 + \frac{0.980}{(L/d)} - \frac{0.133}{(L/d)^2}} \tag{5}$$

$$k_B \tag{6}$$

All of the values, as summarized in Table 1, vary as the length changes. The translational diffusivity D_t, rotational diffusivity D_r, and rotational velocity decrease with increasing length which are easy to understood by the Einstein law; as the length increases, both translational and rotational drag forces increase, which results in a decrease in both the diffusivity and velocity. However, while D_t is quite close to $D_{t,b}$, a discrepancy of several orders of magnitude is observed between D_r and $D_{r,b}$ for longer core-shell NWs. The vortices at the tail of the cathode, found in the numerical modelling (see again Figure 1b) may explain the observed discrepancy between D_r and $D_{r,b}$ for a longer NW. This additional fluidic drag caused by the vortices, electrochemically formed contributes to the large reduction in the rotational diffusivity, hence reducing its tendency to rotate and, therefore, increasing its motion stability (or directionality.) For a detailed elucidation, we example macro-scaled flying objects, such as rockets or airplanes. For those flying objects, it is commonly known that the center of drag force should locate behind the center of thrust for a directional stability, and the stability further increases with the distance of the two centers. In our case, the center of thrust locates at the tip of the anode, while the center of drag force, supposed to be at the center for this rectangular shaped-nanomotor is actually shifted to the side of the cathode tip due to the additional drag force. The distance of the two centers further increases with the size of vortex as the length increases.

In addition, the increase in translational velocity (v) with increasing length is unexpected and somewhat counter-intuitive. Previous study conducted on Cu/Pt nanomotors show a decrease in velocity with increasing nanomotor length, most likely due to the increased drag force for a longer length.[20] However, in our experiments the speed of Au-Ru core-shell nanomotor increased with the nanomotor length, as shown by the averaged measured velocities in Figure 3c for lengths of 1.5, 2.5 and 3.5 µm (N>8 for each length). Our experimental values show a dissimilar trend with the numerical simulations (Figure 1c). The increase in speed with length in the experimental data implies that there might be an extra driving force that increases with length.

This extra driving force superimposes on the main driving force (electroosmotic force), resulting in increase in the net propulsive force of the nanomotor (Figure 3d). We can assume that the extra driving force can be related to a self-diffusiophoresis mechanism because O_2 concentration gradient around the motor surface is reinforced as the catalytically reactive surface area (Ru) increases with length. Although it is intuitively compelling that self-diffusiophoresis due to the generated O_2 concentration on the Ru surface leads to a speed enhancement, the exact magnitude of such enhancement remains unknown, and it is therefore difficult to directly compare the relative contribution from the enhanced force due to O_2 generation, and the larger viscous drag that a longer rod would experience slowing down the motor.

Catalytic propulsion of the core-shell NWs with various material combinations and the prediction of their propulsive force. In order to further investigate the role of diffusiophoresis in the catalytic propulsion of core-shell naonomtors, we fabricated Au/Rh and Rh/Au core-shell NWs with a length of 2.5 um. Their motion in the presence of 20 wt% H_2O_2 were compared with that of Au/Ru core-shell NW. We note that Ru/Au core-shell NW was not fabricated due to the growth limit of Ru cores beyond 200 nm in a length. The trajectories of the core-shell NWs are represented in Figure 4. The speed comparison of these three types of nanomotors was Au/Ru >> Rh/Au > Au/Rh (See the Supplementary movie2).

Such a trend cannot be explained by existing theory on self-electroosmosis, and we reason as follows. The speed of a self-electroosmotic nanomotor is in general correlated to a combination of the surface charge of the nanomotor (zeta potential), and the self-generated electric field as a result of surface electrochemical reactions. To understand the effects of these two factors, we first measured the zeta potential of Au/Ru, Rh/Au and Au/Rh core-shell NWs, all yielding results around ~ -26 mV. This indicates that the observed speed difference among these three samples cannot be explained solely by the differences in their zeta potential. Secondly, as far as self-generated electric field is concerned, we believe that the difference among these three samples are to be insignificant, supported by a previous study by Wang et al.[22] showing similar speed of Au-Ru, Rh-Au and Au-Rh segmented NW motors. To briefly summarize, self-electroosmosis mechanism would predict similar speeds for these three samples, which is in clear contrast to what we have experimentally observed.

Given the inadequacy of self-electroosmosis in explaining the observed speed trend, we attempt to reconcile our results with self-diffusiophoresis. The magnitude of the self-diffusiophoretic force (extra driving force) depends on the O_2 concentration gradient, developed by the decomposition of H_2O_2 on the catalytically active layer. According to the previous studies, the decomposition rate of H_2O_2 on Ru is twice as high as Rh, while it is 10 times slower on Au than on Rh.[55] This implies that the predicted magnitude of the self-diffusiophoretic forces on the core-shell NWs are in the order of Au/Rh >> Rh/Au > Au/Ru core-shell NWs, provided that the total number of H_2O_2 decomposition is defined as the product of the decomposition rate and the reactive surface area. With the regards, diffusiophoretic force directions on Au/Rh, Rh/Au, Au/Ru core-shell nanomotors can be predicted as $Au \rightarrow Rh$, $Rh \rightarrow Au$ and $Au \rightarrow Ru$ respectively. The predicted force magnitudes and directions are illustrated in the left column of Figure 4. We note that the arrow sizes are relative among three core-shell samples.

To this end,, the relative speeds among three nanomotors are predicted by comparing the magnitudes of the propulsive forces that is the sum of the self-electroosmotic force and self-diffusiophoretic force. Since the Au/Ru and Au/Rh core-shell NW exhibits the highest and lowest propulsive force respectively, the expected speeds for the core-shell NWs decrease in the following order: Au/Ru > Rh/Au > Au/Rh. This prediction is in accordance with our experimental observation, confirming our propulsion mechanism.

Magnetic guided motion of (Au-Ni)/Ru core-shell NWs.

In this section, we demonstrate that the trajectory of our core-shell NWs can be controlled under an applied magnetic field in H_2O_2 solution. For a magnetically guided motion, a Ni segment was additionally deposited on a Au segment, and subsequently coated with a Ru shell (see Figure S3 for SEM images and EDX mapping of the (Au-Ni)/Ru core-shell NWs). A magnetic guided motion was performed under the magnetic field ($\vec{B}$) of 1mT with a negligible magnetic field gradient. Supplementary movie 3 shows rectangular trajectories of two (Au-Ni)/Ru core-shell NWs when the field orientation is switched counterclockwise with a step of 90°. Interestingly, the magnetic field only serves to align the motors parallel to the magnetic field lines, but it does not determine the heading direction along them.

In conclusion, core-shell NWs composed Au/Ru have been fabricated and studied as a potential catalytic nanomotor when submerged in H_2O_2. Their maximum speed was observed to be 41±7.6 μm/s at a 20% H_2O_2 concentration. Moreover, decreased rotational diffusivity or, equivalently, enhanced directionality is observed with increased length, which results from the formation of vortices at the end of the cathode as revealed by the electroosmotic mechanism based numerical simulation. Experimentally, this nanomotor design exhibits a positive length-speed correlation, which is contrary to what occurs in other designs or in our simulation. In the case of our core-shell nanostructures, we assume that the propulsion comes from two simultaneous mechanisms: self-diffusiophoresis and self-electroosmosis. When the catalytic active surface area (Ru) increases with length, the self-diffusiophoretic force increases due to a higher O_2 concentration gradient. For a core-shell Au/Ru NW, the generated self-diffusiophoretic force is superimposed to the self-electroosmotic force with the same force direction. Therefore, the net propulsion force is reinforced. The suggested propulsion mechanism also justifies the large difference in speed among Au/Rh, Rh/Au and Au/Ru core-shell NWs, which has not been observed for conventional bimetallic NWs. Finally, we have successfully demonstrated magnetically guided motion of core-shell NWs by inserting a Ni segment in the core-shell architecture as a magnetic responsive material. The core-shell fabrication method presented here also allows for the integration of materials within the shell such as magnetic parts, and prevent them to be in direct contact with the surrounding environment.

Figures

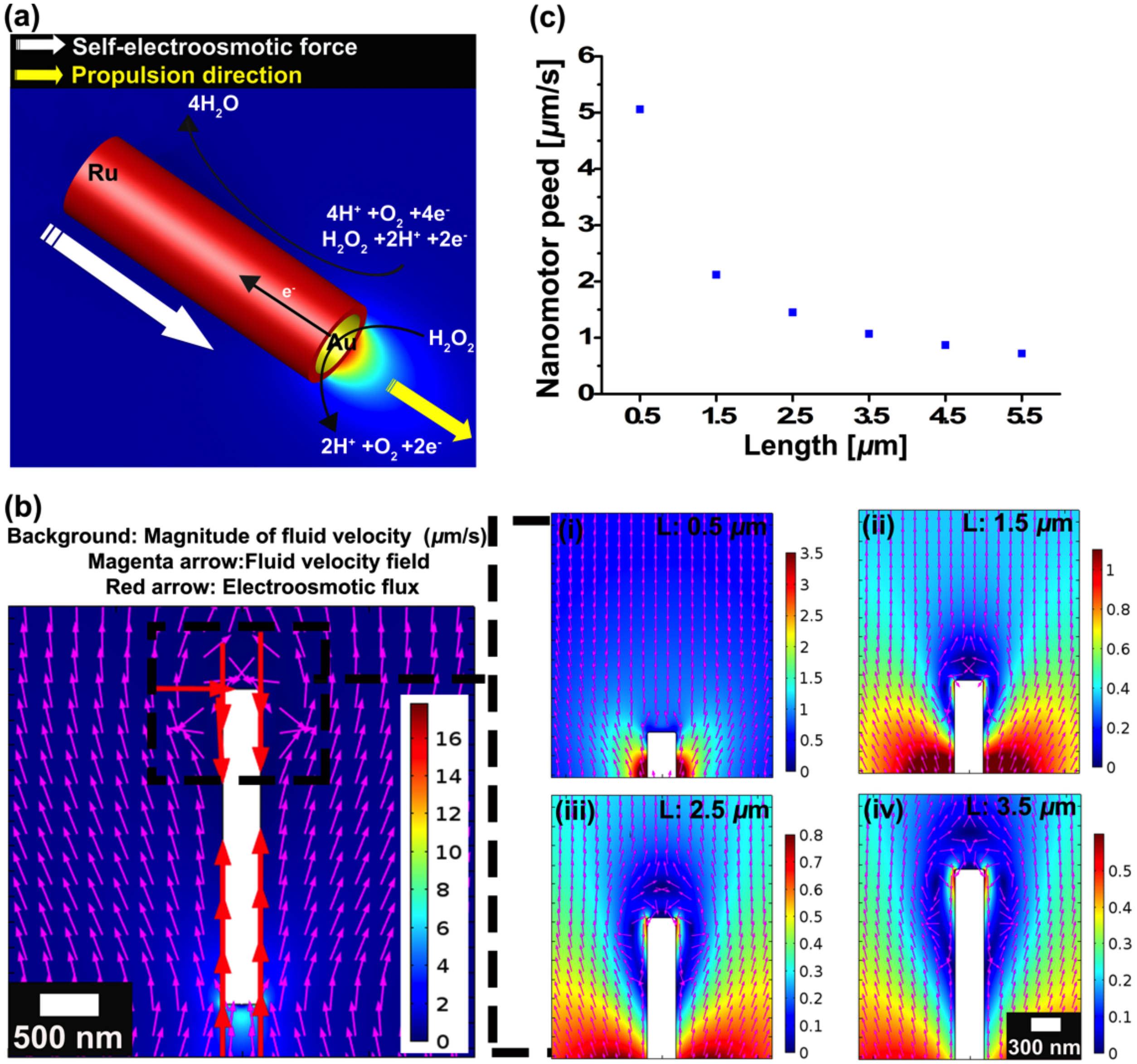

Figure 1. Numerical modeling of Au/Ru core-shell NW in the presence of H_2O_2: (a) A schematic drawing of the self-electroosmotic model for our Au/Ru core-shell NW. We note the force arrow is represented from the point of view of the nanomotor, rather than fluid. b) Magnitude of fluid velocity (background), fluid velocity (magenta arrows) and electroosmotic flux (red arrows) of Au/Ru core-shell NW with a length of 2.5 um; the inserts are the magnified images of the magnitude of fluid velocity (background) and fluid velocity field (magenta arrows) for the length of (i) 0.5 um, (ii) 1.5 um, (iii) 2.5 um and (iv) 3.5 um; the diameter of NWs are fixed to 300 nm, and (c) Speed as a function of lengths.

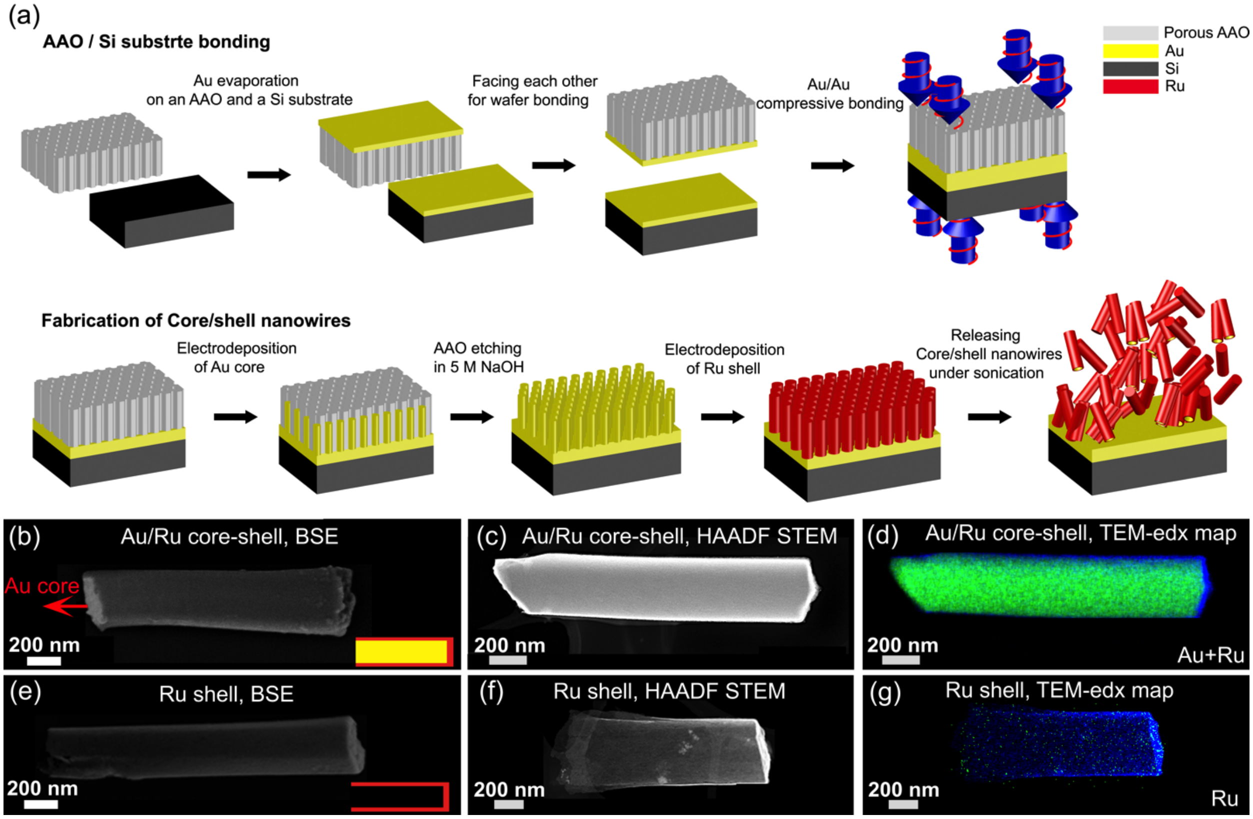

Figure 2. (a) A schematic drawing of the fabrication of core-shell NWs: the fabrication process includes AAO/Si substrate bonding and electrodeposition. BSE images of (b) a Au/Ru core-shell NW and (e) a Ru shell. *Insets in (b) and (e) are schematic drawings of Au/Ru core-shell NW and Ru shell, respectively. HAADF STEM images of (c) a Au/Ru core-shell NW and (f) a Ru shell. TEM-edx maps of (d) a Au/Ru core-shell NW and (g) a Ru shell, respectively.

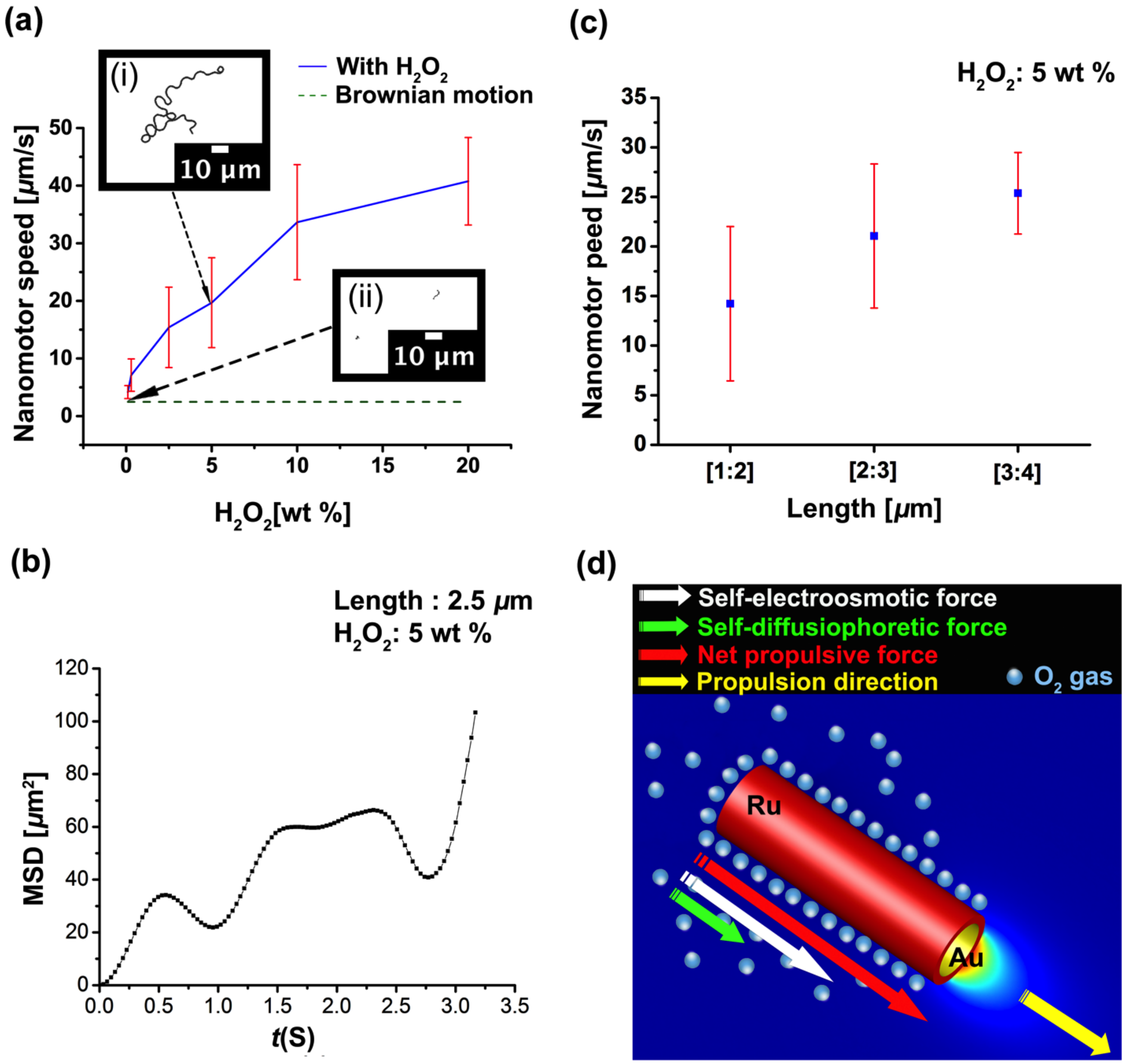

Figure3. Experimental data of Au/Ru core-shell NW in the presence of H_2O_2: (a) Averaged speed as a function of the concentration of H_2O_2. Speed was averaged from at least 11 samples with an approximate length of 2.5 μm. Inset (i): A tracked path of a core-shell NW at 5 wt % H_2O_2. And inset (ii): A tracked path of a core-shell NW at 0 wt % H_2O_2. (b) a MSD curve of Au/Ru core-shell NWs at the approximate length of 2.5 μm. (c) Speed of Au/Ru core-shell NWs as a function of a length of NWs in the presence of 5 wt % H_2O_2. *The length of core-shell NWs ranges from 1 to 2 μm, 2 to 3 μm and 3 to 4 μm. Averaged speed from at least eight samples for each range. (d) A schematic drawing of our proposed mechanism for the propulsion of the Au/Ru core-shell NWs. We note the force arrows are represented from the point of view of the nanomotor, rather than fluid.

Table 1. Measured parameters (D_t, v, D_r and ω) and theoretical values ($D_{t,b}$ and $D_{r,b}$) of Au/Ru core-shell NWs

Parameters **Length**	D_t (μm²/s)	$D_{t,b}$ (μm²/s)	v (μm/s)	D_r (μm²/rad)	$D_{r,b}$ (μm²/rad)	Ω (rad/s)
1.8 μm	0.97	0.71	9.83	1.84	2.13	6.97
2.6 μm	0.58	0.58	16.35	0.44	1.52	5.73
3.4 μm	0.31	0.50	27.88	0.0015	1.18	1.43

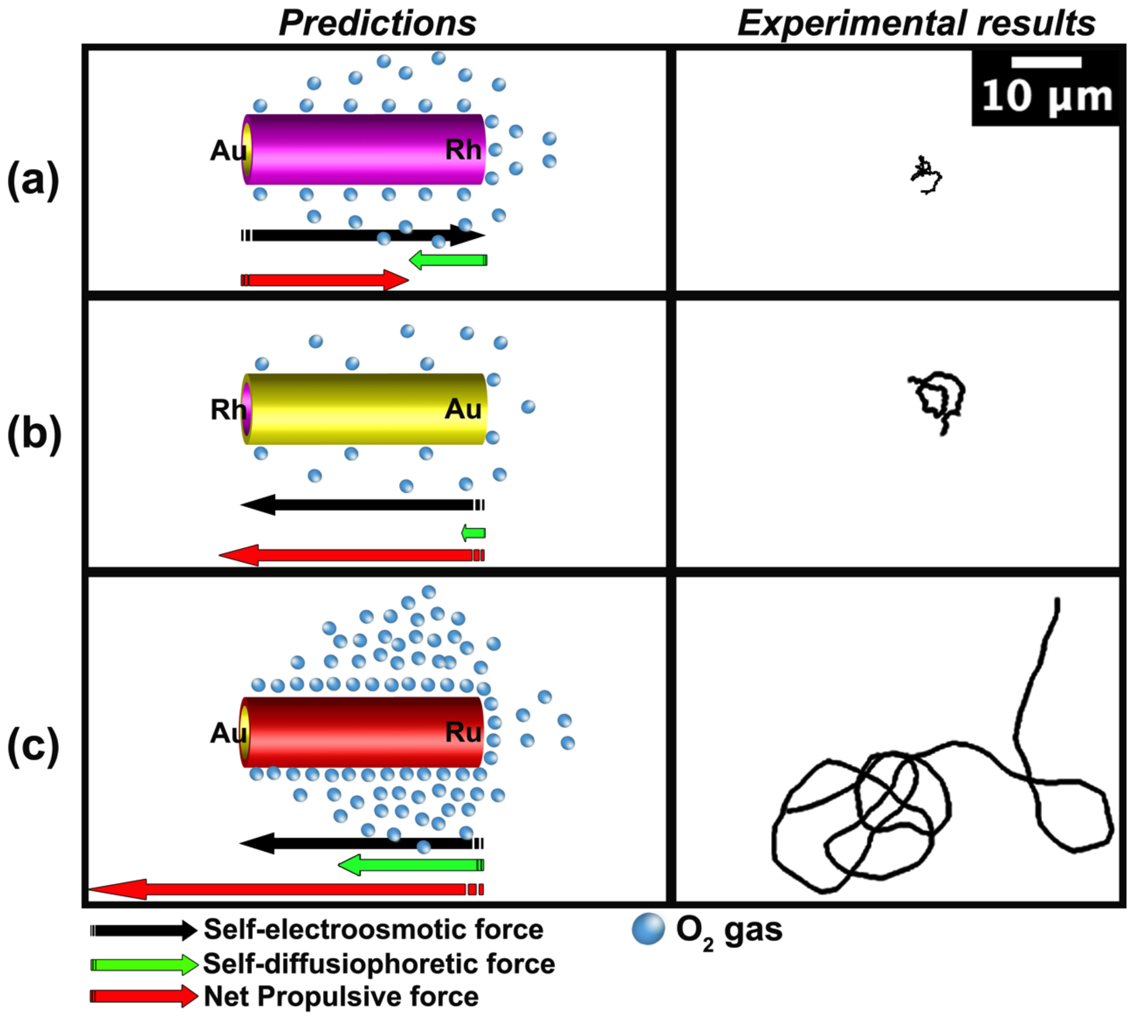

Figure 4. The predictions of the magnitude and direction of self-electroosmotic and self-diffusiophoretic forces, and the experimentally observed tracked paths of (a) Au/Rh, (b) Rh/Au and (c) Au/Ru core-shell NWs over 4.8 sec. * The arrow size are relatively predicted in three samples and force arrows are represented from the point of view of the nanomotor, rather than fluid.

TOC

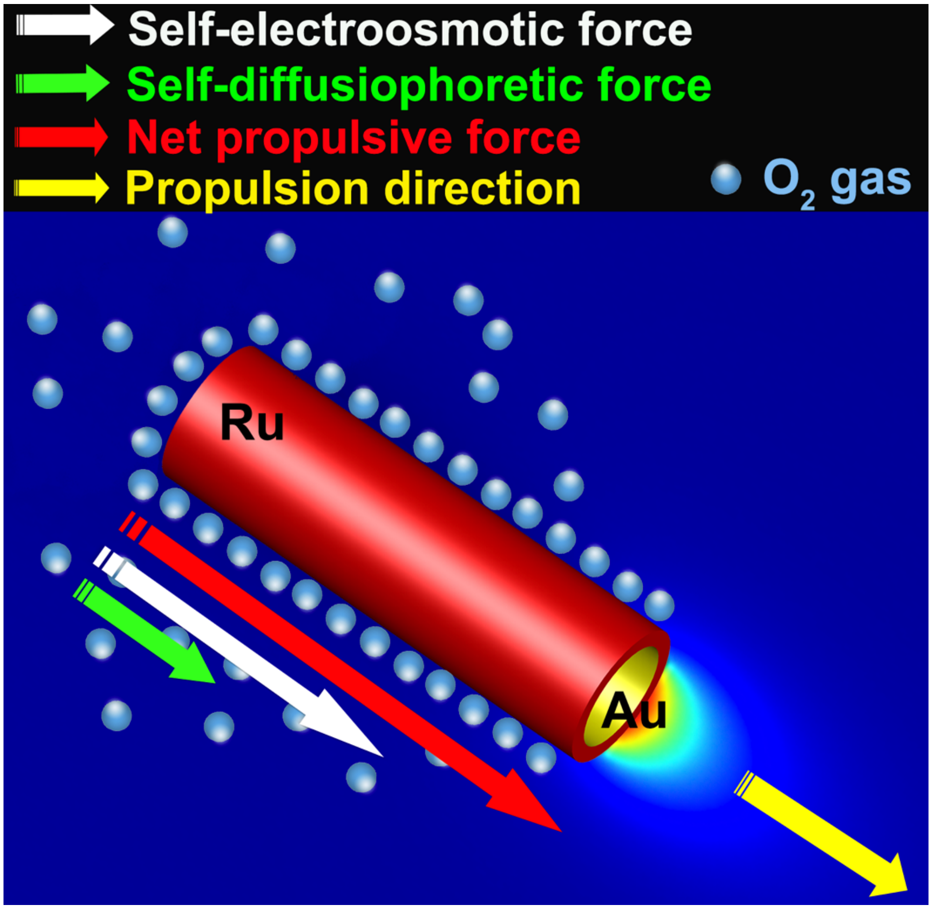
Self-electroosmotic force
Self-diffusiophoretic force
Net propulsive force
Propulsion direction
O_2 gas
Ru
Au

REFERENCES

(1) Ismagilov, R. F.; Schwartz, A.; Bowden, N.; Whitesides, G. M. Autonomous Movement and Self-Assembly. *Angew. Chem. Int. Ed. Engl.* 2002, 41, 652-654.

(2) Wang, W.; Duan, W.; Ahmed, S.; Mallouk, T. E.; Sen, A. Small power: Autonomous nano- and micromotors propelled by self-generated gradients. *Nano Today* 2013, 8, 531-554.

(3) Mano, N.; Heller, A. Bioelectrochemical Propulsion. *J. Am. Chem. Soc.* 2005, 127, 11574-11575.

(4) Ma, X.; Jannasch, A.; Albrecht, U. R.; Hahn, K.; Miguel-Lopez, A.; Schaffer, E.; Sanchez, S. Enzyme-Powered Hollow Mesoporous Janus Nanomotors. *Nano Lett.* 2015, 15, 7043-7050.

(5) Gaspar, S. Enzymatically induced motion at nano- and micro-scales. *Nanoscale* 2014, 6, 7757-7763.

(6) Li, J.; Shklyaev, O. E.; Li, T.; Liu, W.; Shum, H.; Rozen, I.; Balazs, A. C.; Wang, J. Self-Propelled Nanomotors Autonomously Seek and Repair Cracks. *Nano Lett.* 2015, 15, 7077-7085.

(7) Dey, K. K.; Zhao, X.; Tansi, B. M.; Mendez-Ortiz, W. J.; Cordova-Figueroa, U. M.; Golestanian, R.; Sen, A. Micromotors Powered by Enzyme Catalysis. *Nano Lett.* 2015, 15, 8311-8315.

(8) Li, J.; Gao, W.; Dong, R.; Pei, A.; Sattayasamitsathit, S.; Wang, J. Nanomotor lithography. *Nat. Commun.* 2014, 5, 5026.

(9) Kline, T. R.; Paxton, W. F.; Wang, Y.; Velegol, D.; Mallouk, T. E.; Sen, A. Catalytic Micropumps: Microscopic Convective Fluid Flow and Pattern Formation. *J. Am. Chem. Soc.* 2005, 127, 17150-17151.

(10) Sundararajan, S.; Lammert, P. E.; Zudans, A. W.; Crespi, V. H.; Sen, A. Catalytic Motors for Transport of Colloidal Cargo. *Nano Lett.* 2008, 8, 1271-1276.

(11) Dey, K. K.; Wong, F.; Altemose, A.; Sen, A. Catalytic Motors—Quo Vadimus? *Curr. Opin. Colloid Interface Sci.* 2016, 21, 4-13.

(12) Yadav, V.; Duan, W.; Butler, P. J.; Sen, A. Anatomy of Nanoscale Propulsion. *Annu. Rev. Biophys.* 2015, 44, 77-100.

(13) Sanchez, S.; Soler, L.; Katuri, J. Chemically powered micro- and nanomotors. *Angew. Chem. Int. Ed. Engl.* 2015, 54, 1414-1444.

(14) Wang, W.; Duan, W.; Ahmed, S.; Sen, A.; Mallouk, T. E. From one to many: dynamic assembly and collective behavior of self-propelled colloidal motors. *Acc. Chem. Res.* 2015, 48, 1938-1946.

(15) Guix, M.; Mayorga-Martinez, C. C.; Merkoci, A. Nano/micromotors in (bio)chemical science applications. *Chem. Rev.* 2014, 114, 6285-6322.

(16) Zhou, C.; Zhang, H.; Li, Z.; Wang, W. Chemistry pumps: a review of chemically powered micropumps. *Lab Chip* 2016, 16, 1791-1811.

(17) Colberg, P. H.; Reigh, S. Y.; Robertson, B.; Kapral, R. Chemistry in motion: tiny synthetic motors. *Acc. Chem. Res.* 2014, 47, 3504-3511.

(18) Solovev, A. A.; Mei, Y.; Bermudez Urena, E.; Huang, G.; Schmidt, O. G. Catalytic microtubular jet engines self-propelled by accumulated gas bubbles. *Small* 2009, 5, 1688-1692.

(19) Huang, W.; Manjare, M.; Zhao, Y. Catalytic Nanoshell Micromotors. *J. Phys. Chem. C* 2013, 117, 21590-21596.

(20) Liu, R.; Sen, A. Autonomous nanomotor based on copper-platinum segmented nanobattery. *J. Am. Chem. Soc.* 2011, 133, 20064-20067.

(21) Paxton, W. F.; Kistler, K. C.; Olmeda, C. C.; Sen, A.; St. Angelo, S. K.; Cao, Y.; Mallouk, T. E.; Lammert, P. E.; Crespi, V. H. Catalytic Nanomotors: Autonomous Movement of Striped Nanorods. *J. Am. Chem. Soc.* 2004, 126, 13424-13431.

(22) Wang, Y.; Hernandez, R. M.; Bartlett, D. J.; Bingham, J. M.; Kline, T. R.; Sen, A.; Mallouk, T. E. Bipolar Electrochemical Mechanism for the Propulsion of Catalytic Nanomotors in Hydrogen Peroxide Solutions†. *Langmuir* 2006, 22, 10451-10456.

(23) Pumera, M. Electrochemically powered self-propelled electrophoretic nanosubmarines. *Nanoscale* 2010, 2, 1643-1649.

(24) Fournier-Bidoz, S.; Arsenault, A. C.; Manners, I.; Ozin, G. A. Synthetic self-propelled nanorotors. *Chem. Commun.* 2005, 4, 441-443.

(25) Ma, X.; Hahn, K.; Sanchez, S. Catalytic mesoporous Janus nanomotors for active cargo delivery. *J. Am. Chem. Soc.* 2015, 137, 4976-4979.

(26) Yamamoto, D.; Takada, T.; Tachibana, M.; Iijima, Y.; Shioi, A.; Yoshikawa, K. Micromotors working in water through artificial aerobic metabolism. *Nanoscale* 2015, 7, 13186-13190.

(27) Howse, J. R.; Jones, R. A.; Ryan, A. J.; Gough, T.; Vafabakhsh, R.; Golestanian, R. Self-motile colloidal particles: from directed propulsion to random walk. *Phys. Rev. Lett.* 2007, 99, 048102.

(28) Frankel, A. E.; Khair, A. S. Dynamics of a self-diffusiophoretic particle in shear flow. *Phys. Rev. E: Stat., Nonlinear, Soft Matter Phys.* 2014, 90, 013030.

(29) Golestanian, R.; Liverpool, T. B.; Ajdari, A. Propulsion of a molecular machine by asymmetric distribution of reaction products. *Phys. Rev. Lett.* 2005, 94, 220801.

(30) Wilson, D. A.; Nolte, R. J.; van Hest, J. C. Autonomous movement of platinum-loaded stomatocytes. *Nat. Chem.* 2012, 4, 268-274.

(31) Wang, S.; Wu, N. Selecting the swimming mechanisms of colloidal particles: bubble propulsion versus self-diffusiophoresis. *Langmuir* 2014, 30, 3477-3486.

(32) Hu, J.; Odom, T. W.; Lieber, C. M. Chemistry and Physics in One Dimension: Synthesis and Properties of Nanowires and Nanotubes. *Acc. Chem. Res.* 1999, 32, 435-445.

(33) Nicewarner-Pena, S. R.; Freeman, R. G.; Reiss, B. D.; He, L.; Pena, D. J.; Walton, I. D.; Cromer, R.; Keating, C. D.; Natan, M. J. Submicrometer metallic barcodes. *Science* 2001, 294, 137-141.

(34) Ozel, T.; Bourret, G. R.; Mirkin, C. A. Coaxial lithography. *Nat. Nanotechnol.* 2015, 10, 319-324.

(35) Kline, T. R.; Paxton, W. F.; Mallouk, T. E.; Sen, A. Catalytic Nanomotors: Remote-Controlled Autonomous Movement of Striped Metallic Nanorods. *Angew. Chem. Int. Ed. Engl.* 2005, 117, 754-756.

(36) Hangarter, C. M.; Lee, Y. I.; Hernandez, S. C.; Choa, Y. H.; Myung, N. V. Nanopeapods by galvanic displacement reaction. *Angew. Chem. Int. Ed. Engl.* 2010, 49, 7081-7085.

(37) Lauhon, L. J.; Gudiksen, M. S.; Wang, D.; Lieber, C. M. Epitaxial core-shell and core-multishell nanowire heterostructures. *Nature* 2002, 420, 57-61.

(38) Hwang, J.; Min, B.; Lee, J. S.; Keem, K.; Cho, K.; Sung, M. Y.; Lee, M. S.; Kim, S. Al2O3 Nanotubes Fabricated by Wet Etching of ZnO/Al2O3 Core/Shell Nanofibers. *Adv. Mater.* 2004, 16, 422-425.

(39) Yin, Y.; Lu, Y.; Sun, Y.; Xia, Y. Silver Nanowires Can Be Directly Coated with Amorphous Silica To Generate Well-Controlled Coaxial Nanocables of Silver/Silica. *Nano Lett.* 2002, 2, 427-430.

(40) Kong, X. Y.; Ding, Y.; Wang, Z. L. Metal−Semiconductor Zn−ZnO Core−Shell Nanobelts and Nanotubes. *J. Phys. Chem. B* 2004, 108, 570-574.

(41) Cao, H. Q.; Xu, Z.; Sang, H.; Sheng, D.; Tie, C. Y. Template Synthesis and Magnetic Behavior of an Array of Cobalt Nanowires Encapsulated in Polyaniline Nanotubules. *Adv. Mater.* 2001, 13, 121-123.

(42) Hu, J. Q.; Meng, X. M.; Jiang, Y.; Lee, C. S.; Lee, S. T. Fabrication of Germanium-Filled Silica Nanotubes and Aligned Silica Nanofibers. *Adv. Mater.* 2003, 15, 70-73.

(43) Moran, J. L.; Wheat, P. M.; Posner, J. D. Locomotion of electrocatalytic nanomotors due to reaction induced charge autoelectrophoresis. *Phys. Rev. Lett. E* 2010, 81, 065302.

(44) Moran, J. L.; Posner, J. D. Electrokinetic locomotion due to reaction-induced charge auto-electrophoresis. *J. Fluid Mech.* 2011, 680, 31-66.

(45) Wang, W.; Chiang, T. Y.; Velegol, D.; Mallouk, T. E. Understanding the efficiency of autonomous nano- and microscale motors. *J .Am. Chem. Soc.* 2013, 135, 10557-10565.

(46) Jang, B.; Chen, X.-Z.; Siegfried, R.; Montero Moreno, J. M.; Özkale, B.; Nielsch, K.; Nelson, B. J.; Pané, S. Silicon-supported aluminum oxide membranes with ultrahigh aspect ratio nanopores. *RSC Adv.* 2015, 5, 94283-94289.

(47) Hill, J. J.; Haller, K.; Gelfand, B.; Ziegler, K. J. Eliminating capillary coalescence of nanowire arrays with applied electric fields. *ACS Appl. Mater. Interfaces* 2010, 2, 1992-1998.

(48) Marine, N. A.; Wheat, P. M.; Ault, J.; Posner, J. D. Diffusive behaviors of circle-swimming motors. *Phys. Rev. Lett. E* 2013, 87.

(49) Lee, T. C.; Alarcon-Correa, M.; Miksch, C.; Hahn, K.; Gibbs, J. G.; Fischer, P. Self-propelling nanomotors in the presence of strong Brownian forces. *Nano Lett.* 2014, 14, 2407-2412.

(50) Demirok, U. K.; Laocharoensuk, R.; Manesh, K. M.; Wang, J. Ultrafast catalytic alloy nanomotors. *Angew. Chem. Int. Ed. Engl.* 2008, 47, 9349-9351.

(51) Laocharoensuk, R.; Burdick, J.; Wang, J. Carbon-Nanotube-Induced Acceleration of Catalytic Nanomotors. *ACS Nano* 2008, 2, 1069-1075.

(52) Teeffelen, S. V.; Lowen, H. Dynamics of a Brownian circle swimmer. *Phys. Rev. E: Stat., Nonlinear, Soft Matter Phys.* 2008, 78, 020101.

(53) Ebbens, S.; Jones, R. A.; Ryan, A. J.; Golestanian, R.; Howse, J. R. Self-assembled autonomous runners and tumblers. *Phys. Rev. E: Stat., Nonlinear, Soft Matter Phys.* 2010, 82, 015304.

(54) Charsooghi, M. A.; Akhlaghi, E. A.; Tavaddod, S.; Khalesifard, H. R. A MATLAB program to calculate translational and rotational diffusion coefficients of a single particle. *Comput. Phys. Commun.* 2011, 182, 400-408.

(55) McKee, D. W. Catalytic decomposition of hydrogen peroxide by metals and alloys of the platinum group. *J. Catal.* 1969, 14, 355-364.

ASSOCIATED CONTENT

Supporting Information.

Experimental procedures, numerical modelling procedures, supplementary figures and supplementary movies are included.

This material is available free of charge via the Internet at http://pubs.acs.org.

AUTHOR INFORMATION

Corresponding Author

*E-mail: bjang@ethz.ch, vidalp@ethz.ch

Author Contributions

S.P. and B.J.N. initiated the project. S.P. and B.J. designed the fabrication experiments. B.J. and S.W. fabricated the magnetic nanoswimmers and analyzed their motion. W.W. and B.J. conducted the simulation experiments. B.J., W.W., A.P., X.C., B.J.N., D.F. and A.F. performed the analysis of the swimmers and provided theoretical discussion. B.J., W.W., A.P., X.C., S.P., and B.J.N. supervised the work and gave critical input. All authors contributed to discussions.

Notes

The authors declare no competing financial interests.

ACKNOWLEDGMENT

Funding support from the European Community's Seventh Framework Programme (FP7/2007-2013) under grant agreement 296679 (MANAQA) is acknowledged. S.P. acknowledges financial support by the European Research Council Starting Grant "Magnetoelectric Chemonanomotorics for Chemical and Biomedical Applications (ELECTROCHEMBOTS)", by the ERC grant agreement n. 336456. W.W. is grateful for the financial support from National Natural Science Foundation of China (Grant No. 11402069) and the city government of Shenzhen (Grant No. KQCX20140521144102503). We especially thank Prof. Mahmut Selman Sakar from the Mechanical Engineering (School of Engineering, EPFL), and Carlos C.J. Alcantara and Ayoung Hong from the Multi-Scale Robotics Lab (ETH Zürich) for constructive discussions.